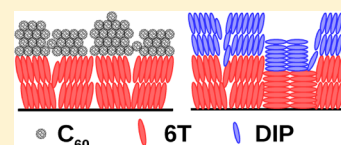


Templating Effects of α -Sexithiophene in Donor–Acceptor Organic Thin Films

C. Lorch,[†] R. Banerjee,^{†,‡} J. Dieterle,[†] A. Hinderhofer,[†] A. Gerlach,^{*,†} J. Drnec,[§] and F. Schreiber[†][†]Universität Tübingen, Institut für Angewandte Physik, Auf der Morgenstelle 10, 72076 Tübingen, Germany[‡]Department of Physics, Indian Institute of Technology Gandhinagar, Ahmedabad 382424, India[§]ESRF – The European Synchrotron, 71 Avenue des Martyrs, 38000 Grenoble, France

ABSTRACT: Small-molecule organic photovoltaic cells often employ a planar heterojunction (PHJ) geometry where the electron donor and acceptor materials are stacked one on top of the other. The thin-film growth scenario of such PHJs can be very different from the one of a single compound on a bare substrate. We have investigated the growth of PHJs, consisting of two different donor–acceptor pairs, namely, α -sexithiophene (6T)/C₆₀ and 6T/diindenoperylene (DIP) using real-time in situ X-ray scattering. For both donor–acceptor material combinations, we observe that the coherent in-plane crystalline size of the second material strongly correlates with the one of the bottom one, and hence a strong templating effect of the 6T on the material deposited subsequently, indicating a strong interaction between the two materials in the PHJ. Furthermore, a change in the structure of the 6T film during the deposition of the second material was observed, which shows that the deposition of an additional material on top of a templating layer can partially change the crystal structure of the templating film itself.



INTRODUCTION

During the past few years the field of organic electronics has strongly emerged. Organic photovoltaic (OPV), organic light-emitting diodes, or organic field-effect transistors (OFETs) are attractive alternatives to their common inorganic counterparts due to low-temperature preparation conditions, relatively low production costs, and the possibility of using flexible substrates.^{1–5} For OPV cells, active layers consisting of only one material are not efficient,⁶ and usually active layers of at least two materials are necessary. In general, one can distinguish between two extreme cases of the geometries of the active organic layers. On the one hand, the active layer may consist of mixtures of an electron donor and an electron acceptor material, called bulk heterojunctions (BHJs), as commonly seen in OPV cells based on polymers.⁷ On the other hand, films with two layers on top of each other, one consisting of an electron donor and the other of an electron acceptor, so-called planar heterojunctions (PHJs), can be used. In reality, solar cells using active-layer geometries between the two extreme cases of a PHJ and a BHJ are also reported.^{8,9} The controlled preparation of films of small molecular compounds via organic molecular beam deposition (OMBD)^{10–12} can be used to prepare PHJs and tailor the film structure so that such OPV cells can exploit features like high exciton diffusion lengths of the compounds.¹⁰ In general, the growth conditions of an organic material on top of another organic compound can be drastically different compared with the growth on, e.g. a native silicon oxide (nSiO) substrate.^{13,14} Epitaxial growth (azimuthal orientation of the top layer following the orientation of the bottom layer)^{15–17} as well as an adoption of the orientation of rod-like molecules in the overlayer (standing-up vs lying-down),¹⁸ are reported.

The material combination of α -sexithiophene (6T) (Figure 1 left) and C₆₀ buckminster fullerene (Figure 1 middle) is an

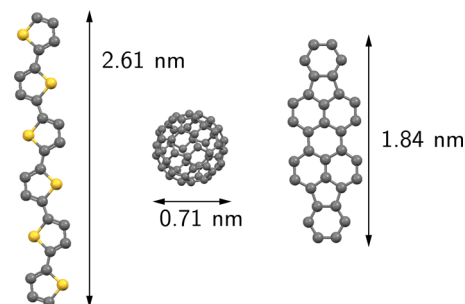


Figure 1. Schematics of the different molecules used in this study. 6T (C₂₄H₁₄S₆) on the left (size from ref 33). In the center C₆₀ (size from refs 34 and 35) and on the right DIP (C₃₂H₁₆) (size from ref 36).

interesting donor–acceptor pair for OPV cells.^{19,20} Interestingly, for this material combination as well as for the combination of 6T and diindenoperylene (DIP) as donor–acceptor pair, a dependence of the open-circuit voltage on the relative orientation and structure of the molecules, together with surface morphologies of similar organic blends, has been reported.²¹ For BHJs of 6T and C₆₀ or C₇₀, postpreparation treatments such as annealing were used to improve the solar cell parameters, but no changes in the structure are reported.^{22,23} Furthermore, the 6T in combination with C₆₀ was used as one of the first ambipolar OFETs.²⁴ The growth of C₆₀ on one or two monolayers of 6T prepared in a lying-down orientation follows a self-organized mechanism in stable chains and chain arrays.^{25–28} For the same configuration on Ag

Received: June 24, 2015

Revised: August 28, 2015

Published: September 14, 2015

Table 1. Crystal Structures of 6T, C₆₀, and DIP

	<i>a</i> (nm)	<i>b</i> (nm)	<i>c</i> (nm)	α (deg)	β (deg)	γ (deg)
6T LT phase ³³	4.4708	0.7851	0.6029	90.00	90.76	90.00
6T β phase ^{47,48}	0.5667	0.7800	4.7288	90.00	100.6	90.00
C ₆₀ fcc ⁴⁹	1.4156	1.4156	1.4156	90.00	90.00	90.00
DIP ⁵⁰	0.709	0.867	1.690	90.00	92.2	90.00

substrates, a charge transfer from the substrate directly to the C₆₀ through the neutral 6T has been reported.^{29,30}

For 6T OPV cells using the PHJ geometry, an extraordinarily high open-circuit voltage, utilizing DIP (Figure 1 right) as electron-acceptor material, is reported.²⁰ In contrast with the sphere-like C₆₀, the perylene derivate DIP is rod-like and hence sterically more compatible to 6T. DIP itself has shown interesting effects as a templating layer, that is, improving the crystal structure of C₆₀ deposited on top³¹ or leading to a void-filling growth scenario of perfluoropentacene (PFP) on DIP³² and also exhibiting a strong templating effect on PFP.¹³

For both OPVs and OFETs the crystalline structure of the films is highly relevant for the efficiency of the device. As shown for other material combinations, the impact of the bottom (organic) material has a huge influence on the film formation process of the material deposited on top.^{13,31,32,37} In situ X-ray diffraction experiments provide an ideal tool to investigate the thin film structure. Because the experiments are performed under ultra-high-vacuum (UHV) conditions, effects from exposure to ambient conditions, possibly changing the film structure, can be precluded. Additionally, real-time experiments allow us to follow the dynamics of structure formation and the investigation of transient effects.^{38–41}

In this study we focus on the correlation of the growth conditions to the overall structure of the PHJ. We prepared different layers of 6T on nSiO, in order to investigate the influence of these templating layers on the growth behavior of C₆₀ and DIP. For the preparation of the 6T films different substrate temperatures and film thicknesses were used, whereas for the growth of C₆₀ only the substrate temperature, and hence the kinetics of the growth, was varied. Similarly, the growth of DIP was studied for different substrate temperatures during the evaporation of the materials.

For both acceptor materials, C₆₀ as well as DIP, when deposited on top of 6T, we observe a strong correlation between the coherently scattering in-plane island size between the templating 6T layer and the top material. Furthermore, the C₆₀ crystal structure improves drastically when deposited on top of 6T compared with nSiO, showing the importance of the surface interaction on the growth of small molecular compounds. In addition, the deposition of the top material modifies the structure of the templating 6T layer, indicating that postgrowth treatment can impact the film structure.

EXPERIMENTAL SECTION

6T was purchased from Sigma-Aldrich and purified twice by temperature gradient sublimation before usage. C₆₀ was purchased from Creaphys and used without further purification. DIP was received from PAH Forschung Greifenberg (Germany). The samples were prepared and measured in a portable UHV chamber.⁴² Before the installation the silicon substrates with a native oxide layer (nSiO) of ~ 1.8 nm were cleaned in an ultrasonic bath with acetone, isopropanol, and purified water. Before each sample preparation the substrates were heated to ~ 770 K to remove the old film. The base

pressure of the system was below 10^{-9} mbar, increasing to $\sim 3 \times 10^{-9}$ mbar during the evaporation of the materials. The evaporation rate, monitored with a water-cooled quartz crystal microbalance, calibrated via X-ray reflectivity (XRR), varied between 0.13 and 0.16 nm/min. The temperature of the substrates was controlled and kept constant via a combination of resistive heating and liquid nitrogen cooling.

The substrate temperatures and other parameters used for the thin-film growth are given in Tables 2 and 3, respectively. The experiments using C₆₀ were performed at the ID03 beamline at the European Synchrotron Radiation Facility (ESRF) using an energy of 11.0 keV ($\lambda = 1.126$ Å) and a four chip MaxiPix area detector.⁴³ The DIP sample series was prepared and measured at the MS-X04SA/Surface Diffraction beamline at the Swiss Light Source (SLS)⁴⁴ using an energy of 12.4 keV ($\lambda = 0.999$ Å) and a PILATUS II area detector. In both cases, slits directly in front of the detector were used to mimic a 0D point detector. The critical angles of the C₆₀/6T/nSiO and DIP/6T/nSiO systems are $\alpha_c = 0.15^\circ$. The incidence angle used for all of the in-plane measurements was $\alpha_i = 0.13^\circ$. Real-time XRR of the deposition of C₆₀ on the 6T templating layers was also performed. The duration of one scan was ~ 190 s, which corresponds approximately to a thickness difference of 0.5 nm per scan. For DIP on 6T, we performed real-time GIXD measurements. The time span between successive scans was 6 min, which corresponds to a time-resolution of ~ 1.0 nm/scan. The Bragg peaks were fitted with Gaussians, and Scherrer's formula was used to estimate the coherently scattering in-plane or out-of-plane crystalline size $D_{\text{coh}} = 2\pi \cdot 0.94/\text{fwhm}$, where 0.94 is Scherrer's constant for spherical crystallites and fwhm is the full width at half-maximum of the fitted peaks. Note that no broadening due to the experimental setup is included in any calculations of the coherently scattering island size, and hence the reported values have to be seen as lower limits. The XRR data were fitted with the Parratt formalism⁴⁵ using the GenX software.⁴⁶ The Kiessig oscillations in the low- q_z region of the films were used to calculate the total film thickness. For the designation of the different peaks, the crystal structures listed in Table 1 were used.

RESULTS AND DISCUSSION

C₆₀ on 6T. For the investigation of the growth behavior of C₆₀ on 6T layers, the growth parameters of the latter were varied, resulting in films with different crystal structures and surface roughnesses. We prepared three different types of templating layer: (a) 5 nm of 6T grown at 373 K gives a well ordered, almost purely β phase, (b) 20 nm of 6T grown at 373 K is dominated by the LT phase and has relatively low amount of β phase domains, (c) 20 nm of 6T grown at 308 K are dominated by the β phase with smaller domain size.

For the C₆₀ we decided to investigate two different substrate temperatures (308 and 203 K). 308 K was chosen to mimic a room-temperature growth, as often employed in organic thin-film growth. Because of the strong templating effect observed at 308 K, additional experiments at 203 K were performed to

reduce the diffusion length of the C_{60} molecules on the surface and see whether the templating effect is still as strong as observed for 308 K.

Characterization of the Templating Layers. For the investigation of the growth behavior of C_{60} on 6T layers, the growth parameters of the latter were varied, resulting in films with different crystal structures and surface roughnesses. The substrate temperature during the deposition was varied between 308 and 373 K, and the films grown at 373 K were prepared with two different nominal thicknesses (5 and 20 nm). This resulted in thin films with different templating layers, as summarized in Table 2.

The templates were characterized using X-ray reflectivity (XRR) and grazing incidence X-ray diffraction (GIXD). For XRR the momentum transfer has only a non-zero out-of-plane component (q_z) that is perpendicular to the sample surface; therefore, this technique probes the out-of-plane film structure. Information on the crystallinity, electron density profile, film thickness, and roughness can be extracted.^{51–53} On the contrary, GIXD is used to probe the in-plane structure of a thin film and q_{xy} is the in-plane momentum transfer.^{51–53} Figure 2a,c shows the data for the XRR and GIXD, respectively. Thicker 6T films show high out-of-plane order, as evidenced by out-of-plane Bragg peaks at either $q_z = 0.28, 0.56,$ and 0.84 \AA^{-1} for the 20.9 nm 373 K film or $q_z = 0.266$ and 0.513 \AA^{-1} for the 17.0 nm 308 K film (Figure 2a).

The Parratt fits are shown as solid lines in Figure 2a. The nominally 5.0 nm film was fitted to 0.4 \AA^{-1} . From the extracted electron density profile (Figure 2b) we see that this film consists of two monolayers, each 2.64 nm thick. This is very close to the value reported for the size of a single 6T molecule.^{17,33} This indicates that the molecules arrange in an almost upright standing orientation. This is in agreement with our previous results that 6T tends to form crystallites of the β phase close to the substrate.⁵⁴ Because the film consists of only two monolayers we assume that it comprises mostly of β phase domains. The top surface is smooth with a roughness of only 0.3 nm. The GIXD data (in-plane) (Figure 2c) show only Bragg peaks that can be associated with the β phase, and peaks that originate from the LT phase (like 6T LT (0 1 1) and (0 2 1)) are not observed. This confirms the estimation that the film consists of only β phase crystallites, which is in agreement with real-time growth results, showing that close to the substrate the film growth is dominantly in the β phase.⁵⁴

Thicker films (nominally 20 nm) were prepared at two different substrate temperatures, 373 and 308 K. The film structure is in agreement with previous reports.⁵⁴ The out-of-plane data of the film prepared at 373 K (black curve in Figure 2) show only damped, weak oscillations in the low- q_z range, indicating a roughness of 5.3 nm. The XRR data are dominated mostly by Bragg reflections of the LT phase. The extracted electron density profile (Figure 2b) shows that the film consists of five completely full layers and eight partially filled layers on top, constituting the roughness and an island-like growth. The thickness of one single molecule layer is 2.29 nm, which corresponds very well to the value reported for the LT phase.³³ The in-plane data reveal that there are crystallites of the β phase; however, the reflections belonging to the LT phase are dominant. The films prepared at 308 K are different from the high-temperature films. Here the structure is dominated by the β phase but the roughness is similar to the one of the 373 K film. In this case the extracted electron density profile (Figure 2b) indicates that the film consists of four completely filled

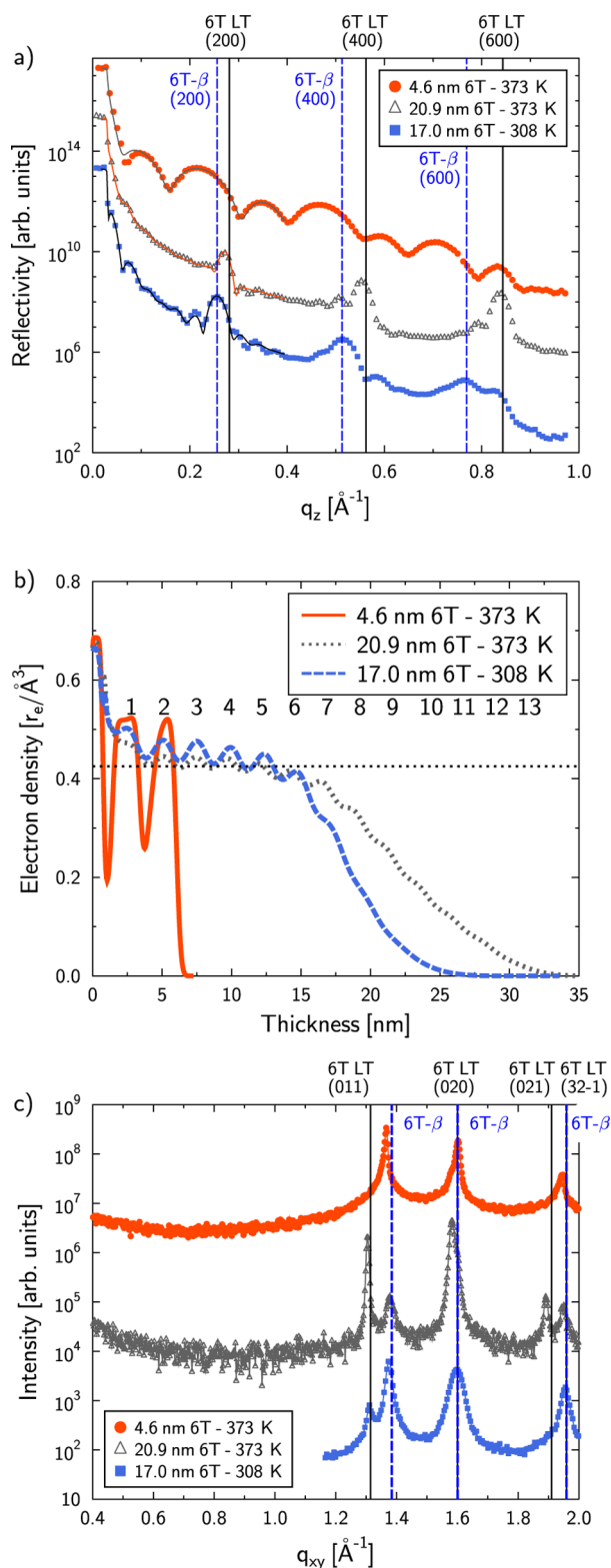


Figure 2. (a) XRR and (c) GIXD data of the templating layers used for the growth of C_{60} . The solid line in panel a corresponds to the fit of the data using Parratt's formalism. Panel b shows the extracted electron density profile of the different films; the numbers refer to layers of 6T, and the dotted horizontal line indicates the difference between completely and only partially filled layers. The curves in panels a and c are shifted for clarity.

layers and six incompletely filled layers, where the latter are less filled compared with the ones of the 373 K film. The monolayer

thickness extracted from the fit is 2.44 nm, which is close to the value reported for the β phase.⁴⁷ The in-plane data show weak reflections that can be associated with the LT phase. To summarize, the three different templating layers have different crystal structures (also in different quality) and roughnesses. There are three different scenarios: The 5 nm thin film consists purely of the β phase and is very smooth. The nominal 20 nm film prepared at 373 K is dominated by the LT phase and the roughness is significantly higher than the one of the 5 nm. The 303 K film has more domains of the β phase than of the LT phase, and the roughness is similar to the one of the high-temperature film.

C_{60} Films on Top of 6T Templates. On the different templating layers previously described, C_{60} films with a nominal thickness of 20 nm were deposited. The substrate temperature, and hence also the temperature of the 6T film, were set to 308 K for all but one film, for which a substrate temperature of 203 K was used. XRR (GIXD) data of the resulting films are presented in Figure 3a,b. For comparison, data of a 20 nm C_{60} film deposited straight on nSiO (green crosses) are also shown alongside. XRR of pure C_{60} does not show clear Bragg reflections consistent with a polycrystalline growth without any

preferential direction on nSiO.³¹ The in-plane data of C_{60} on nSiO show relatively broad Bragg reflections, which can be related to the fcc structure of C_{60} .⁴⁹ In thin-film growth on weakly interacting substrates like nSiO, C_{60} usually grows polycrystalline without a preferred orientation, which can explain the relatively broad peaks.³¹ As soon as a 6T template is used, the out-of-plane structure of the C_{60} improves drastically. The data for films with 6T below the C_{60} in Figure 3a all show a reflection corresponding to the C_{60} (1 1 1) fcc at $q_z = 0.768 \text{ \AA}^{-1}$. The coherently scattering out-of-plane domain size $D_{\text{coh},\perp}$ of C_{60} was estimated by fitting the C_{60} (1 1 1) Bragg peak. The film parameters are summarized in Table 2.

Table 2. Summary of the 6T– C_{60} Film Parameters^a

6T					C_{60}			
T (K)	d (nm)	σ (nm)	$D_{\text{coh},\parallel}$ 6T-LT (nm)	$D_{\text{coh},\parallel}$ 6T- β (nm)	T (K)	d (nm)	$D_{\text{coh},\perp}$ (nm)	$D_{\text{coh},\parallel}$ (nm)
373	4.6	0.3	n.a.	54.7	308	20.3	21.3	52.7
373	4.6	0.3	n.a.	50.4	203	15.2	12.3	11.9
373	20.9	5.3	75.7	n.a.	308	15.0	17.8	69.4
308	17.0	3.3	n.a.	25.1	308	20.2	19.9	35.1
n.a.	n.a.	n.a.	n.a.	n.a.	308	17.6	n.a.	8.0

^aParameters of the different templating layers: substrate temperature, T , thickness, d , roughness, σ , and coherently scattering in-plane domain size, $D_{\text{coh},\parallel}$, of the LT and β phases. The parameters of the C_{60} layers on the templating layers: substrate temperature, T , thickness, d , coherently scattering out-of-plane domain size, $D_{\text{coh},\perp}$, and coherently scattering in-plane domain size, $D_{\text{coh},\parallel}$, calculated from the width of the (2–2 0) Bragg peak.

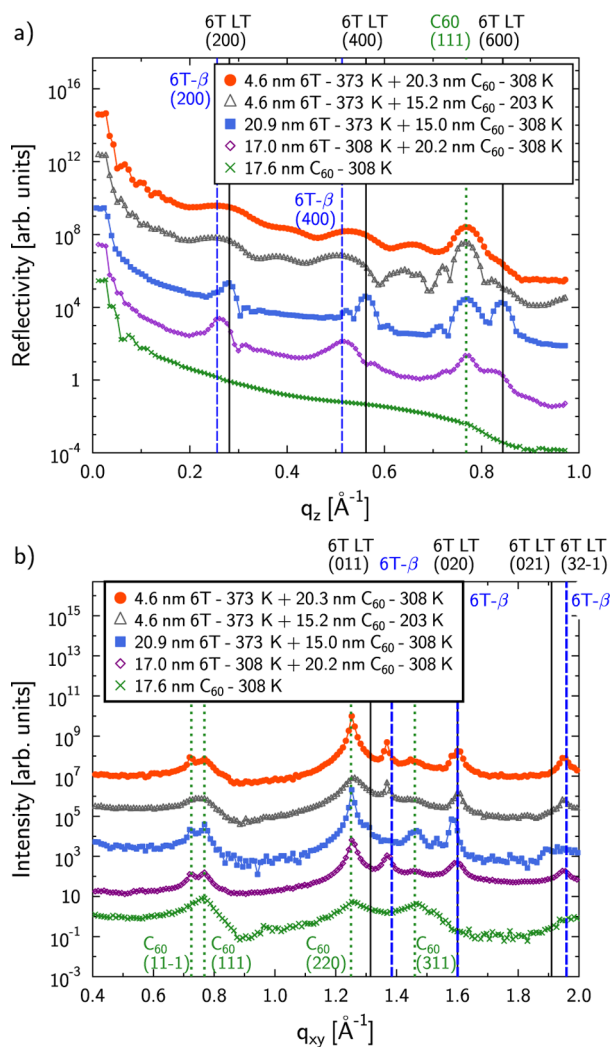


Figure 3. (a) XRR and (b) GIXD data of nominally 20 nm C_{60} deposited on the template layers, respectively. Curves are shifted for clarity.

The highest out-of-plane coherently scattering island size (21.3 nm) is obtained for films prepared at 308 K on a templating layer of 5 nm grown at 373 K. Comparing $D_{\text{coh},\perp}$ to the estimated film thickness of C_{60} , one sees that the two values are very similar, indicating that the coherently scattering crystallites are formed over the whole film thickness. For the same templating parameters, $D_{\text{coh},\perp}$ is significantly smaller ($D_{\text{coh},\perp} = 12.3 \text{ nm}$) when the substrate temperature is set to 203 K; however, the estimated film thickness is also smaller, showing that still the crystallites grow over a relatively wide thickness range. Basically, the whole film is already ordered quite well perpendicular to the substrate surface; increasing the thickness of the templating layer does not show any further improvement ($D_{\text{coh},\perp} = 17.8 \text{ nm}$ for a C_{60} thickness of 15.0 nm). For the C_{60} film on top of the 308 K 6T film the fitted C_{60} Bragg peak is strongly distorted by the third-order Bragg peak of the underlying 6T β phase; therefore, both Bragg peaks were fitted. Also, in this case, the estimated $D_{\text{coh},\perp} = 19.9 \text{ nm}$ coincides very well with the estimated C_{60} thickness of 20.2 nm.

We performed real-time XRR during the deposition of C_{60} on the 5 nm 6T template at 203 and 308 K to see the evolution of the C_{60} structure and monitor potential changes in the underlying template layer during the C_{60} deposition. The data are depicted in Figure 4. For both substrate temperatures, the C_{60} Bragg peak starts to evolve after the deposition of $\sim 2 \text{ nm}$. (For out-of-plane Bragg diffractions, at least two coherently scattering layers are necessary.) So C_{60} grows on the template with a well-ordered crystal structure. Furthermore, a shift of the 6T Bragg reflection around $q_z = 0.5 \text{ \AA}^{-1}$ is observed, which corresponds to the second-order Bragg peak of the β phase, with increasing amount of deposited C_{60} . In the case of the 203

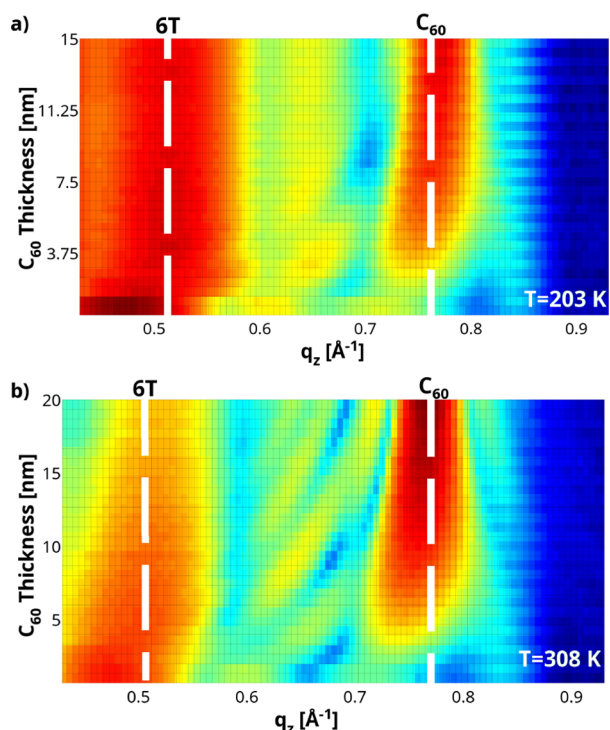


Figure 4. Real-time XRR data of the deposition of C_{60} on 5 nm of 6T at a substrate temperature of (a) 203 and (b) 308 K. The time step between two successive scans was 190 s, which corresponds to 0.5 nm deposited C_{60} . The labels 6T and C_{60} indicate the Bragg peak positions of the 6T- β (4 0 0) and the C_{60} (1 1 1) reflections, respectively. Note that C_{60} thickness can be transcribed to growth time.

K film the Bragg peak is shifted from 0.470 to 0.504 \AA^{-1} (corresponding to a shift from 2.68 to 2.49 nm in real space), and in the 308 K film, the shift is from 0.474 to 0.515 \AA^{-1} (out-of-plane repeat distance changes from 2.65 to 2.44 nm), respectively. In both cases, the q_z value of the Bragg peak is close to the one expected for the β phase (q_z of the (4 0 0) β -peak should be 0.513 \AA^{-1}). Most likely, the additional C_{60} is slightly compressing the underlying 6T, leading to a small change of the 6T tilt angle and hence the layer distance.

The in-plane structure of the different C_{60} films was characterized via GIXD (Figure 3b). Beside the Bragg reflections of the 6T templating layers (previously described) Bragg peaks that can be assigned to the C_{60} fcc structure are observed.⁴⁹

Overall, the C_{60} Bragg peaks on 6T templates are relatively sharp. For the films prepared at 308 K on a templating layer, a peak at $q_{xy} = 0.725 \text{ \AA}^{-1}$ is observed, which is not visible for the pure C_{60} or the film grown at a substrate temperature of 203 K . From reports of C_{60} on DIP templating layers,³¹ we conclude that this peak is the projection of the C_{60} (1 1-1) peak onto the q_{xy} plane and hence an indicator of very well-aligned crystalline domains within the C_{60} .

For a more detailed investigation, the 6T and the C_{60} in-plane coherently scattering crystal size $D_{\text{coh}\parallel}$ was calculated from the widths of the Bragg peaks. The values for the 6T LT (0 1 1) peak, the 6T peak at $q_{xy} = 1.38 \text{ \AA}^{-1}$ corresponding to the β phase, and the C_{60} (2-2 0) are listed in Table 2. By comparing the values of the 6T crystallites to those of the C_{60} layer, one sees that the crystallites of both materials are of similar size in the in-plane direction. It seems that for 373 K this effect is independent of the type of crystal structure of the

bottom layer; for example, β phase versus LT-crystal phase. For the case when the substrate temperature during the C_{60} deposition is only 203 K (on the nSiO), $D_{\text{coh}\parallel}$ of C_{60} is smaller than that for the other films and also significantly smaller than $D_{\text{coh}\parallel}$ of the 6T templating layer; however, the crystallite size (11.9 nm) is still larger than the value of pure C_{60} at 308 K ($D_{\text{coh}\parallel} \approx 8.0 \text{ nm}$). In general, the 6T template layers improve the crystallinity of the C_{60} for all preparation conditions. The C_{60} tends to organize in crystal domains with the (1 1 1) plane parallel to the substrate surface. $D_{\text{coh}\parallel}$ of the C_{60} and that of the 6T are very similar, indicating that there is a strong templating effect of the underlying 6T on the C_{60} .

DIP on 6T. Characterization of the Templating Layers. For the investigation of the templating effects of 6T on the rod-like molecule DIP, three different layers of 6T were prepared. The 6T film structure was modified by altering the substrate temperature during the growth. XRR and GIXD data of the templating layers prepared at 373 K (red circles), 308 K (black triangles), and 233 K (blue squares) are shown in Figure 5a,b, respectively. The thickness of all templating layers was nominally 20 nm . The film parameters of the templating layers are summarized in Table 3, and the structures of the films are similar to the ones described in the C_{60} on 6T Section and in

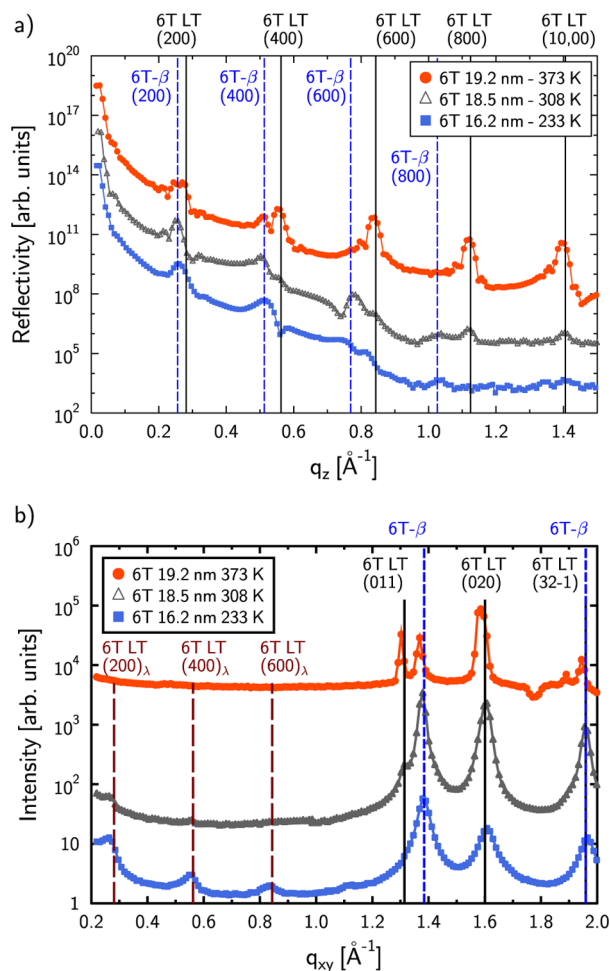


Figure 5. (a) XRR and (b) GIXD data of the 6T templating layers used for the growth of DIP. The curves are shifted with respect to each other for clarity. The annotations with a small λ indicate a lying-down orientation of 6T and the other ones correspond to Bragg peaks of standing-up oriented domains. Adapted from ref 54.

the literature.⁵⁴ In summary, three templating layers with different structural properties are identified: (a) films prepared at 373 K, consisting mainly of the 6T LT phase and having a large $D_{\text{coh}\parallel}$, (b) films prepared at 308 K, showing mainly β phase domains and $D_{\text{coh}\parallel}$ is roughly half the size of $D_{\text{coh}\parallel}$ of the 373 K film, and (c) films prepared at 233 K with even smaller $D_{\text{coh}\parallel}$ and additional fractions of lying-down oriented 6T. The contact plane of the lying-down 6T cannot be unambiguously determined; it could either be the (0 1 0) or the (-4 1 1) plane, which are also reported for lying-down 6T on Cu (1 1 0).⁵⁵

DIP Films on Top of 6T. To investigate the influence of the 6T templating layer on the growth of DIP, we prepared DIP layers with a nominal thickness of 20 nm on top of the 6T layers. The substrate temperature during the deposition of the DIP was the same as the one used for the preparation of the templating layers, that is, 233, 308, and 373 K, respectively. Figure 6a,b shows the XRR and GIXD data of the complete heterostructures, respectively. The 373 K film shows Bragg reflections at $q_z = 0.37$ and 0.74 \AA^{-1} that corresponds to the standing-up (σ -orientation) of DIP.³⁶ In the 308 K film the weak out-of-plane Bragg peaks of the σ -orientation DIP imply that the out-of-plane order of the DIP film is significantly

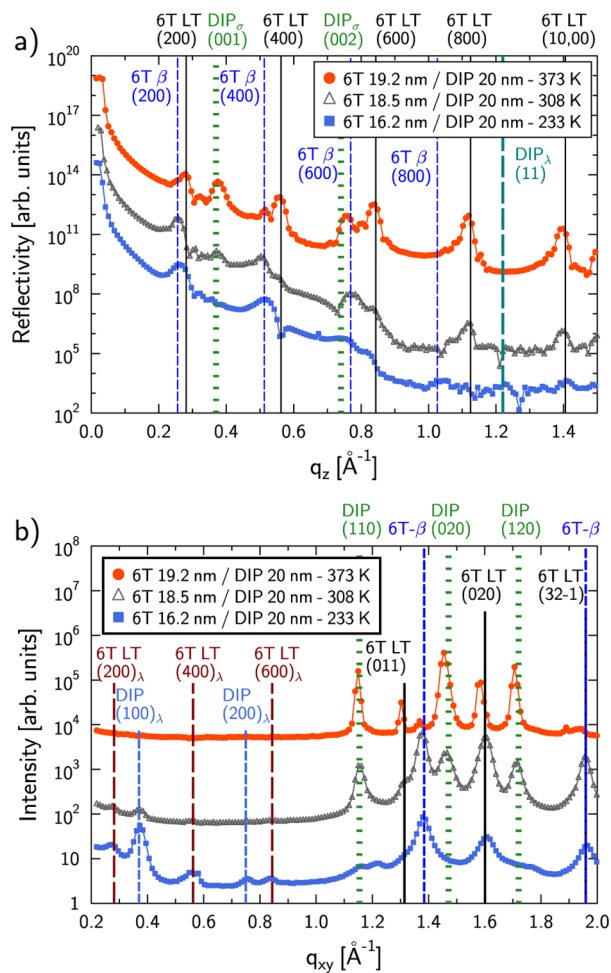


Figure 6. (a) XRR and (b) GIXD data of nominally 20 nm DIP films prepared at 233, 308, and 373 K substrate temperature on 6T layers. Peaks labeled with a small λ correspond to lying-down oriented molecules, whereas peaks of standing-up oriented molecules have either no or a small σ label. Curves are shifted for clarity.

smaller than in the 373 K film. At low substrate temperature, 233 K, the XRR data do not show any indications of standing-up DIP at all. The very weak reflection at $q_z = 1.22 \text{ \AA}^{-1}$ stems from a lying orientation of the DIP.⁵⁶

Table 3. Summary of the 6T–DIP Film Parameters^a

T (K)	6T			DIP			
	d (nm)	σ (nm)	$D_{\text{coh}\parallel}$ 6T $_{\lambda}$	$D_{\text{coh}\parallel}$ 6T $_{\sigma}$	$D_{\text{coh}\parallel}$ 6T- β	$D_{\text{coh}\parallel}$ DIP $_{\lambda}$	$D_{\text{coh}\parallel}$ DIP $_{\sigma}$
373	19.2	3.1	n.a.	44.0	n.a.	n.a.	40.5
308	18.5	3.1	14.3	n.a.	20.5	15.2	21.1
233	16.2	3.8	15.4	n.a.	15.4	17.0	10.3

^aParameters of the different templating layers: substrate temperature, T , film thickness, d , roughness, σ , and in-plane coherently scattering domain sizes, $D_{\text{coh}\parallel}$, of the lying 6T (6T $_{\lambda}$ – (2 0 0) $_{\lambda}$ peak), the 6T-LT phase ((0 1 1) peak), and the 6T β phase (peak at $q_{xy} = 1.38 \text{ \AA}^{-1}$). Parameters of the DIP layer: $D_{\text{coh}\parallel}$ of lying-down oriented molecules (DIP $_{\lambda}$ – (0 0 1) $_{\lambda}$ peak) and of standing-up oriented molecules (DIP $_{\sigma}$ – (1 1 0) peak).

The in-plane data of the 6T/DIP films (Figure 6b) indicate similar orientation of the molecules, as obtained from the XRR data. $D_{\text{coh}\parallel}$ values extracted from the data are summarized in Table 3. For the lying 6T (λ -orientation) the (2 0 0) peak at $q_{xy} = 0.27 \text{ \AA}^{-1}$, for the lying DIP (λ -orientation) the (0 0 1) peak at $q_{xy} = 0.37 \text{ \AA}^{-1}$, for the 6T β phase the peak at $q_{xy} = 1.38 \text{ \AA}^{-1}$, for the standing-up orientation of the 6T LT phase the (0 1 1) peak at $q_{xy} = 1.30 \text{ \AA}^{-1}$, and for the standing DIP molecules (σ -orientation) the (1 1 0) peak at $q_{xy} = 1.16 \text{ \AA}^{-1}$ was considered, respectively. The 373 K film shows only reflections stemming from crystallites comprising standing-up oriented molecules. $D_{\text{coh}\parallel}$ of the standing-up molecules for 6T and DIP is very similar for this film. Interestingly, the ratio of the intensities of the 6T LT (0 1 1) and the 6T β (at $q_{xy} = 1.38 \text{ \AA}^{-1}$) reflections in the final heterostructure is quite different compared with the pure templating layer. In the latter (Figure 5b), both peaks show very similar intensities; however, in the film with DIP on top, the LT peak is significantly stronger than the β peak. This is most likely due to an annealing effect on the pure 6T because the sample was kept at 373 K for ~ 130 min (duration of the postgrowth measurements and of the preparation for the DIP deposition). We will discuss the transition between the two crystal structures in detail later with the real-time data taken during DIP deposition. A small fraction of the 308 K film consists of lying-down molecules, indicated by the small peaks in the low- q_{xy} range. $D_{\text{coh}\parallel}$ for 6T and DIP lying-down domains is very similar (14.3 and 15.2 nm, respectively). The peak with the highest intensity corresponding to the 6T layer is the one of the standing-up β phase. Furthermore, peaks corresponding to standing-up orientation of DIP (at $q_{xy} = 1.15, 1.46$, and 1.71 \AA^{-1}) are observed. Again, $D_{\text{coh}\parallel}$ of the standing-up orientation of 6T and DIP is very similar (20.5 and 21.1 nm). The films prepared at 233 K show relatively strong reflections in the low- q_{xy} range, stemming from domains of lying-down 6T and DIP. Also, in this case, $D_{\text{coh}\parallel}$ of 6T and DIP is very similar; however, the intensity of the lying-down DIP domains is significantly higher than the one of 6T and also than the intensity of the standing-up DIP. This indicates that most of the DIP is arranged in a lying-down orientation. Standing-up molecules of the 6T are found only in the β structure, and very weak peaks of standing-up DIP indicate that only a small fraction of this

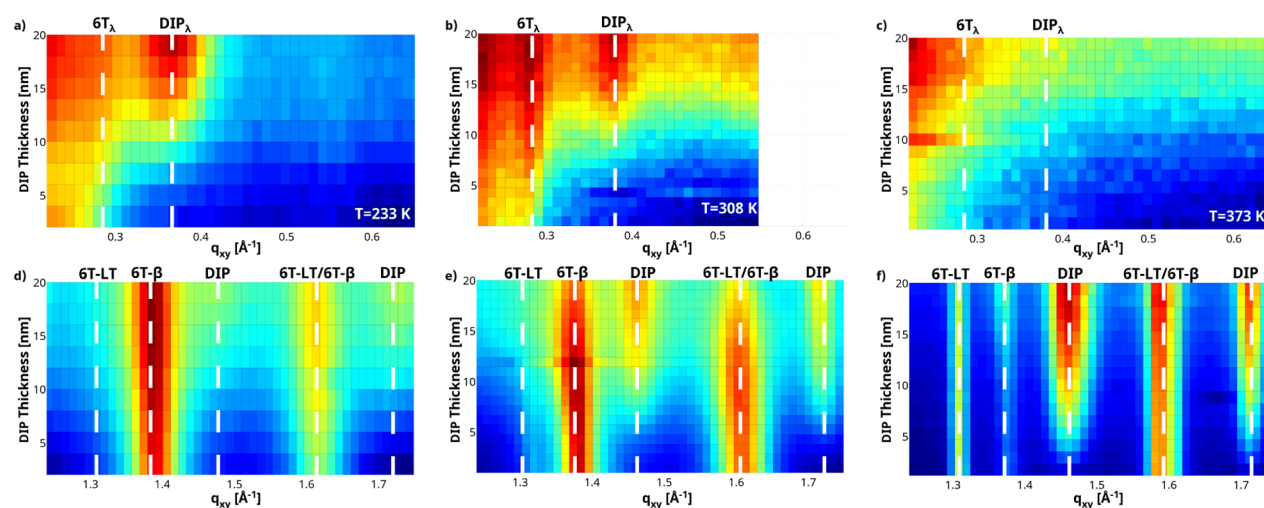


Figure 7. Real-time GIXD data taken during the deposition of the DIP deposition on 6T. (a), (b) and (c) depict the q_{xy} range which shows the evolution of the lying-down orientation of the molecules for 233 K, 308 and 373 K substrate temperature, respectively. $6T_{\lambda}$ ($q_{xy} = 0.28 \text{ \AA}^{-1}$ (2 0 0) LT phase) and DIP_{λ} ($q_{xy} = 0.37 \text{ \AA}^{-1}$ (1 0 0)) indicate the positions of Bragg peaks corresponding to lying-down molecules of the materials. (d), (e) and (f) show the q_{xy} range where reflections of molecules in the standing-up orientation are detected for 233 K, 308 and 373 K substrate temperature, respectively. Here 6T-LT ($q_{xy} = 1.31 \text{ \AA}^{-1}$ (0 1 1) LT phase) and 6T- β indicates Bragg peak positions which can be unambiguously associated with the 6T LT and β phase, respectively, whereas the peak at $q_{xy} = 1.6 \text{ \AA}^{-1}$ can be associated either with the LT ((0 2 0) reflection) or the β phase. The DIP label indicates Bragg peak positions of standing-up DIP molecules ($q_{xy} = 1.46 \text{ \AA}^{-1}$ (0 2 0) and $q_{xy} = 1.71 \text{ \AA}^{-1}$ (1 2 0)). Note that DIP thickness can be transcribed to growth time.

orientation is present in the film. $D_{\text{coh||}}$ of standing-up 6T and DIP is again of similar magnitudes (15.4 and 10.3 nm).

In general, we have seen that low substrate temperatures promote the growth of lying-down DIP, whereas high substrate temperatures lead to better ordered DIP films (e.g., higher $D_{\text{coh||}}$) with a standing-up orientation. This is similar to results reported for DIP on nSiO.⁵⁰ Interestingly, for all substrate temperatures and both orientations (standing-up and lying-down), there is a strong correlation of $D_{\text{coh||}}$ between the templating 6T layer and the top DIP layer. This leads to the proposition that the domains of DIP are arranged in the same orientation as the underlying 6T domains, that is, lying-down DIP on lying-down 6T and standing-up DIP on standing-up 6T.

For a better understanding of the templating effect on the growth process of the overlayer, we performed real-time GIXD scans during the deposition of the DIP layer. Two different q_{xy} ranges (0.2 to 0.7 \AA^{-1} and 1.25 to 1.8 \AA^{-1}) were measured alternately and are shown in Figure 7. In the top row (a–c) the data of the first q_{xy} range and in the second row (d–f) the data of the second q_{xy} range are plotted, respectively. For the 233 K film, mainly the evolution of the lying DIP can be followed (Figure 7a). After ~ 24 min (~ 5 nm) of film growth the formation of the Bragg peak starts to appear, indicating the formation of crystalline domains. The DIP (0 0 1) $_{\lambda}$ peak gets stronger and sharper over the whole growth process.

The signal of the DIP standing-up domains (Figure 7d) is relatively weak. For films at 308 K, the growth of the lying-down DIP is quite similar to the one of the film prepared at 233 K. For the first 5 nm of growth, no indications of lying-down DIP can be found (Figure 7d), and only after this thickness do crystallites start to form. Nevertheless, the intensity of the corresponding DIP Bragg peak is only increasing slowly, and, as already mentioned, the intensity at the end of the film growth is significantly lower than the one in the 233 K film. The standing-up oriented DIP molecules start to form domains only after ~ 5 nm, as evidenced by the formation of the DIP (0 2 0)

and (1 2 0) peak at $q_{xy} = 1.46$ and 1.71 \AA^{-1} , respectively. During the growth, $D_{\text{coh||}}$ of the DIP (0 2 0) and (1 2 0) peaks increases from 12.5 to 16.0 nm and 13.5 to 21.6 nm, respectively (blue symbols in Figure 8).

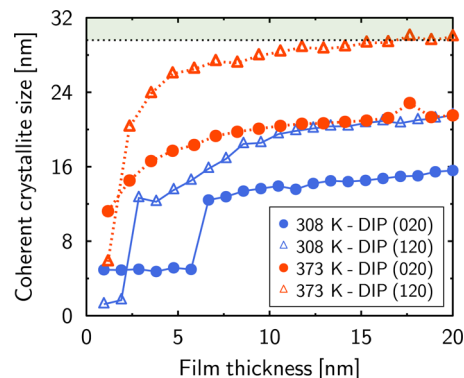


Figure 8. Evolution of the coherently scattering island sizes for the DIP (0 2 0) and (1 2 0) reflections of the films prepared at 308 and 373 K substrate temperature. The shaded area indicates the resolution limit of the DIP (1 2 0) peak.

At a substrate temperature of 373 K, no domains with lying-down oriented molecules can be observed (Figure 7c). The (0 1 1) 6T LT phase peak ($q_{xy} = 1.30 \text{ \AA}^{-1}$) stays constant during the whole film growth; however, the intensity of the Bragg peak corresponding to the 6T β phase ($q_{xy} = 1.38 \text{ \AA}^{-1}$) increases during the DIP deposition. At the beginning of the DIP deposition this peak is almost not visible, which is contrary to the postgrowth characterization of the 6T templating layer. As previously mentioned, this might be explained by a postgrowth annealing. Then, during the DIP deposition, the intensity of the β phase Bragg peak starts to increase again after 10 nm deposition of DIP, showing that domains corresponding to the 6T β phase start evolving again; however, $D_{\text{coh||}}$ of the 6T β

phase is not changing. In contrast with the films prepared at lower substrate temperature, in the case of 373 K the DIP crystallites of the σ -orientation are formed almost immediately after the start of the deposition; already after the growth of one monolayer, reflections from DIP are observed. During further growth, the intensities of the DIP Bragg peaks increase with more amount of material being deposited, but the fwhm of the peaks is not changing significantly. During the first 5 nm of growth $D_{\text{coh||}}$ of the DIP (0 2 0) and (1 2 0) peaks increases to ~ 20 and ~ 30 nm and then stay more or less constant for the rest of the film growth (red symbols in Figure 8). Please note that $D_{\text{coh||}}$ of the DIP (1 2 0) peak after a film thickness of ~ 20 nm is resolution-limited (shaded area in Figure 8) and therefore we cannot rule out a larger $D_{\text{coh||}}$.

Discussion. The results of the bilayers of 6T and C_{60} as well as of 6T and DIP have shown that 6T has a strong templating effect on both materials used as top-layer. The in-plane coherently scattering size $D_{\text{coh||}}$ of the templating 6T layers and the one of the material deposited on top show a strong correlation, indicating that generally the top material seems to adopt the configuration of the bottom material and forms nicely organized domains right on top of the crystallites of the templating layer. C_{60} on 6T seems to partially organize itself from the beginning with its (1 1 1) plane parallel to the substrate plane instead of growing with completely randomly oriented domains, most likely due to a different surface potential distribution of the 6T layer compared with nSiO. This also results in a better defined out-of-plane structure of the film. At lower substrate temperatures (203 K) the templating effect is still observed; however, it is not as pronounced as observed for the films prepared at 308 or 373 K. At 203 K the thermal energy provided by the substrate is not enough to allow the C_{60} to diffuse on the substrate surface to find a potential minimum on-top of the 6T.

A templating effect of DIP is also observed on 6T. Because the coherent domain sizes of the underlying 6T and the DIP deposited on top are very similar, we expect a growth scenario where the DIP crystallites are formed directly on top of the respective domains below. Both materials deposited on top, C_{60} and DIP, act as electron acceptor in contact with 6T and hence form donor–acceptor pairs with the latter.²⁰ In such pairs charge-transfer mechanisms are likely to occur and usually lead to relatively strong coupling between the molecules. This might be the reason for the orientational templating of DIP on 6T and the well-oriented growth of C_{60} on 6T, which was already reported also for DIP¹⁵ and pentacene.⁵⁷

Furthermore, the structural change of the bottom 6T templating layer during the deposition of DIP at 373 K indicates that organic thin films are sensitive to post-growth treatment. In this case the additional material leads to a partial reorganization of the 6T layer, wherein domains of the LT structure change into domains of the β phase, which is not a pure annealing effect because this transition is not observed for 6T films without a DIP overlayer; however, the structural change of the 6T layer during the deposition of C_{60} (decrease in the out-of-plane repeat distance) is similar to an annealing effect where 6T domains are transformed into the thermodynamically more stable LT phase.

CONCLUSIONS

In conclusion, we have investigated the growth of the electron donor–acceptor pairs 6T– C_{60} and 6T–DIP by means of X-ray scattering techniques in real-time and in situ. For both material

combinations a very strong correlation between the coherently scattering domain size of the templating 6T layer and of the acceptor material is observed. This pronounced templating effect might be attributed to a strong interaction between the materials, potentially by a charge transfer from the donor to the acceptor material. The deposition of C_{60} on top of 6T has a similar effect as an annealing step of pure 6T. Furthermore, the reappearance of the β phase crystallites in the 6T bottom layer during the deposition of DIP indicates that postgrowth treatment of an organic thin film, in our case the deposition of an additional organic semiconductor on top, can, under certain circumstances, change the original layer structure.

AUTHOR INFORMATION

Corresponding Author

*E-mail: alexander.gerlach@uni-tuebingen.de.

Notes

The authors declare no competing financial interest.

ACKNOWLEDGMENTS

We gratefully acknowledge the MS-X04SA/Surface Diffraction beamline staff for their assistance during experiments at the Swiss Light Source and the ID03 beamline staff at the ESRF for their assistance during the experiments there. This work was supported by the German Research Foundation (DFG) within the priority program SPP 1355 “Elementary Processes of Organic Solar Cells” and by the Baden-Württemberg Stiftung in the program “Organic Photovoltaics and Dye Sensitized Solar Cells”. C.L. thanks the Carl-Zeiss-Stiftung for funding and R.B. acknowledges funding by HYMEC.

REFERENCES

- (1) *Physics of Organic Semiconductors*, 2nd ed.; Brütting, W.; Adachi, C., Eds.; Wiley VCH-Verlag: Weinheim, Germany, 2012.
- (2) Forrest, S. R. The path to ubiquitous and low-cost organic electronic appliances on plastic. *Nature* **2004**, *428*, 911–918.
- (3) Bernède, J. C. Organic photovoltaic cells: History, principle and techniques. *J. Chil. Chem. Soc.* **2008**, *53*, 1549–1564.
- (4) Kelley, T. W.; Baude, P. F.; Gerlach, C.; Ender, D. E.; Muyres, D.; Haase, M. A.; Vogel, D. E.; Theiss, S. D. Recent progress in organic electronics: Materials, devices, and processes. *Chem. Mater.* **2004**, *16*, 4413–4422.
- (5) Farchioni, R.; Grosso, G. *Organic Electronic Materials*; Springer-Verlag: Berlin, Germany, 2001.
- (6) Tang, C. W. Two-layer organic photovoltaic cell. *Appl. Phys. Lett.* **1986**, *48*, 183–185.
- (7) Dyakonov, V. Mechanisms controlling the efficiency of polymer solar cells. *Appl. Phys. A: Mater. Sci. Process.* **2004**, *79*, 21–25.
- (8) Wagner, J.; Gruber, M.; Hinderhofer, A.; Wilke, A.; Bröker, B.; Frisch, J.; Amsalem, P.; Vollmer, A.; Opitz, A.; Koch, N.; et al. High fill factor and open circuit voltage in organic photovoltaic cells with diindenopyrene as donor material. *Adv. Funct. Mater.* **2010**, *20*, 4295–4303.
- (9) Opitz, A.; Wagner, J.; Brütting, W.; Salzmann, I.; Koch, N.; Manara, J.; Pflaum, J.; Hinderhofer, A.; Schreiber, F. Charge separation at molecular donor-acceptor interfaces: correlation between morphology and solar cell performance. *IEEE J. Sel. Top. Quantum Electron.* **2010**, *16*, 1707–1717.
- (10) Schreiber, F. Organic molecular beam deposition: Growth studies beyond the first monolayer. *phys. stat. sol. (a)* **2004**, *201*, 1037–1054.
- (11) Kowarik, S.; Gerlach, A.; Schreiber, F. Organic molecular beam deposition: Fundamentals, growth dynamics, and in-situ studies. *J. Phys.: Condens. Matter* **2008**, *20*, 184005(1–12).

- (12) Forrest, S. R. Ultrathin organic films grown by organic molecular beam deposition and related techniques. *Chem. Rev.* **1997**, *97*, 1793–1896.
- (13) Hinderhofer, A.; Hosokai, T.; Frank, C.; Novák, J.; Gerlach, A.; Schreiber, F. Templating effect for organic heterostructure film growth: Perfluoropentacene on diindenoperylene. *J. Phys. Chem. C* **2011**, *115*, 16155–16160.
- (14) Yang, J.; Yan, D.; Jones, T. S. Molecular Template Growth and Its Applications in Organic Electronics and Optoelectronics. *Chem. Rev.* **2015**, *115*, 5570–5603.
- (15) Oehzelt, M.; Koller, G.; Ivanco, J.; Berkebile, S.; Haber, T.; Resel, R.; Netzer, F. P.; Ramsey, M. G. Organic heteroepitaxy: p-sexiphenyl on uniaxially oriented α -sexithiophene. *Adv. Mater.* **2006**, *18*, 2466–2470.
- (16) Koller, G.; Berkebile, S.; Krenn, J. R.; Netzer, F. P.; Oehzelt, M.; Haber, T.; Resel, R.; Ramsey, M. G. Heteroepitaxy of organic-organic nanostructures. *Nano Lett.* **2006**, *6*, 1207–1212.
- (17) Djuric, T.; Hernandez-Sosa, G.; Schwabegger, G.; Koini, M.; Hesser, G.; Arndt, M.; Brinkmann, M.; Sitter, H.; Simbrunner, C.; Resel, R. Alternately deposited heterostructures of α -sexithiophene-para-hexaphenyl on muscovite mica(001) surfaces: crystallographic structure and morphology. *J. Mater. Chem.* **2012**, *22*, 15316–15325.
- (18) Heutz, S.; Cloots, R.; Jones, T. S. Structural templating effects in molecular heterostructures grown by organic molecular-beam deposition. *Appl. Phys. Lett.* **2000**, *77*, 3938–3940.
- (19) Veenstra, S.; Malliaras, G.; Brouwer, H.; Esselink, F.; Krasnikov, V.; van Hutten, P.; Wildeman, J.; Jonkman, H.; Sawatzky, G.; Hadziioannou, G. Sexithiophene- C_{60} blends as model systems for photovoltaic devices. *Synth. Met.* **1997**, *84*, 971–972.
- (20) Hörmann, U.; Wagner, J.; Gruber, M.; Opitz, A.; Brütting, W. Approaching the ultimate open circuit voltage in thiophene based single junction solar cells by applying diindenoperylene as acceptor. *Phys. Status Solidi RRL* **2011**, *5*, 241–243.
- (21) Hörmann, U.; Lorch, C.; Hinderhofer, A.; Gerlach, A.; Gruber, M.; Kraus, J.; Sykora, B.; Grob, S.; Linderl, T.; Wilke, A.; et al. V_{OC} from a morphology point of view: The Influence of molecular orientation on the open circuit voltage of organic planar hetero-junction solar cells. *J. Phys. Chem. C* **2014**, *118*, 26462–26470.
- (22) Alem, S.; Pandey, A. K.; Unni, K. N. N.; Nunzi, J.-M.; Blanchard, P. Molecular model T6: C_{60} bulk-heterojunction solar cells. *J. Vac. Sci. Technol., A* **2006**, *24*, 645–648.
- (23) Sakai, J.; Taima, T.; Yamanari, T.; Saito, K. Annealing effect in the sexithiophene: C_{70} small molecule bulk heterojunction organic photovoltaic cells. *Sol. Energy Mater. Sol. Cells* **2009**, *93*, 1149–1153.
- (24) Dodabalapur, A.; Katz, H. E.; Torsi, L.; Haddon, R. C. Organic heterostructure field-effect transistors. *Science* **1995**, *269*, 1560–1562.
- (25) Zhang, H. L.; Chen, W.; Chen, L.; Huang, H.; Wang, X. S.; Yuhara, J.; Wee, A. T. S. C_{60} molecular chains on α -sexithiophene nanostripes. *Small* **2007**, *3*, 2015–2018.
- (26) Chen, L.; Chen, W.; Huang, H.; Zhang, H.; Yuhara, J.; Wee, A. Tunable arrays of C_{60} molecular chains. *Adv. Mater.* **2008**, *20*, 484–488.
- (27) Huang, H.; Chen, W.; Chen, L.; Zhang, H. L.; Wang, X. S.; Bao, S. N.; Wee, A. T. S. Zigzag C_{60} chain arrays. *Appl. Phys. Lett.* **2008**, *92*, 023105 (1–3).
- (28) Wang, R.; Mao, H. Y.; Huang, H.; Qi, D. C.; Chen, W. Scanning tunneling microscopy and photoelectron spectroscopy investigation of the sexithiophene: C_{60} donor-acceptor nanostructure formation on graphite. *J. Appl. Phys.* **2011**, *109*, 084307–1–084307–5.
- (29) Niederhausen, J.; Amsalem, P.; Wilke, A.; Schlesinger, R.; Winkler, S.; Vollmer, A.; Rabe, J. P.; Koch, N. Doping of C_{60} (sub)monolayers by Fermi-level pinning induced electron transfer. *Phys. Rev. B: Condens. Matter Mater. Phys.* **2012**, *86*, 081411 (1–5).
- (30) Amsalem, P.; Niederhausen, J.; Wilke, A.; Heimel, G.; Schlesinger, R.; Winkler, S.; Vollmer, A.; Rabe, J. P.; Koch, N. Role of charge transfer, dipole-dipole interactions, and electrostatics in Fermi-level pinning at a molecular heterojunction on a metal surface. *Phys. Rev. B: Condens. Matter Mater. Phys.* **2013**, *87*, 035440 (1–13).
- (31) Hinderhofer, A.; Gerlach, A.; Broch, K.; Hosokai, T.; Yonezawa, K.; Kato, K.; Kera, S.; Ueno, N.; Schreiber, F. Geometric and electronic structure of templated C_{60} on diindenoperylene thin films. *J. Phys. Chem. C* **2013**, *117*, 1053–1058.
- (32) Hinderhofer, A.; Gerlach, A.; Kowarik, S.; Zontone, F.; Krug, J.; Schreiber, F. Smoothing and coherent structure formation in organic-organic heterostructure growth. *Euro Phys. Lett.* **2010**, *91*, S6002(1–5).
- (33) Horowitz, G.; Bachet, B.; Yassar, A.; Lang, P.; Demanze, F.; Fave, J.-L.; Garnier, F. Growth and characterization of sexithiophene single crystals. *Chem. Mater.* **1995**, *7*, 1337–1341.
- (34) Yannoni, C. S.; Bernier, P. P.; Bethune, D. S.; Meijer, G.; Salem, J. R. NMR determination of the bond lengths in C_{60} . *J. Am. Chem. Soc.* **1991**, *113*, 3190–3192.
- (35) Adams, G. B.; Page, J. B.; Sankey, O. F.; Sinha, K.; Menendez, J.; Huffman, D. R. First-principles quantum molecular-dynamics study of the vibrations of icosahedral C_{60} . *Phys. Rev. B: Condens. Matter Mater. Phys.* **1991**, *44*, 4052–4055.
- (36) Dürr, A. C.; Schreiber, F.; Münch, M.; Karl, N.; Krause, B.; Kruppa, V.; Dosch, H. High structural order in thin films of the organic semiconductor diindenoperylene. *Appl. Phys. Lett.* **2002**, *81*, 2276–2278.
- (37) Hinderhofer, A.; Schreiber, F. Organic-organic heterostructures: Concepts and applications. *ChemPhysChem* **2012**, *13*, 628–643.
- (38) Krause, B.; Schreiber, F.; Dosch, H.; Pimpinelli, A.; Seeck, O. H. Temperature dependence of the 2D-3D transition in the growth of PTCDA on Ag(111): A real-time X-ray and kinetic Monte Carlo study. *Europhys. Lett.* **2004**, *65*, 372–378.
- (39) Kowarik, S.; Gerlach, A.; Sellner, S.; Schreiber, F.; Cavalcanti, L.; Kononov, O. Real-time observation of structural and orientational transitions during growth of organic thin films. *Phys. Rev. Lett.* **2006**, *96*, 125504(1–4).
- (40) Frank, C.; Banerjee, R.; Oettel, M.; Gerlach, A.; Novák, J.; Santoro, G.; Schreiber, F. Analysis of island shape evolution from diffuse x-ray scattering of organic thin films and implications for growth. *Phys. Rev. B: Condens. Matter Mater. Phys.* **2014**, *90*, 205401(1–10).
- (41) Bommel, S.; Kleppmann, N.; Weber, C.; Spranger, H.; Schäfer, P.; Novak, J.; Roth, S.; Schreiber, F.; Klapp, S.; Kowarik, S. Unravelling the multilayer growth of the fullerene C_{60} in real time. *Nat. Commun.* **2014**, *5*, 5388(1–8).
- (42) Ritley, K. A.; Krause, B.; Schreiber, F.; Dosch, H. A portable ultrahigh vacuum organic molecular beam deposition system for *in situ* x-ray diffraction measurements. *Rev. Sci. Instrum.* **2001**, *72*, 1453–1457.
- (43) Ponchut, C.; Rigal, J. M.; Clément, J.; Papillon, E.; Homs, A.; Petitdemange, S. MAXIPIX, a fast readout photon-counting X-ray area detector for synchrotron applications. *J. Instrum.* **2011**, *6*, C01069 (1–10).
- (44) Willmott, P. R.; Meister, D.; Leake, S. J.; Lange, M.; Bergamaschi, A.; Böge, M.; Calvi, M.; Cancellieri, C.; Casati, N.; Cervellino, A.; et al. The Materials Science beamline upgrade at the Swiss Light Source. *J. Synchrotron Radiat.* **2013**, *20*, 667–682.
- (45) Parratt, L. G. Surface studies of solids by total reflection of X-rays. *Phys. Rev.* **1954**, *95*, 359–369.
- (46) Björck, M.; Andersson, G. GenX: An extensible X-ray reflectivity refinement program utilizing differential evolution. *J. Appl. Crystallogr.* **2007**, *40*, 1174–1178.
- (47) Servet, B.; Ries, S.; Trotel, M.; Alnot, P.; Horowitz, G.; Garnier, F. X-ray determination of the crystal structure and orientation of vacuum evaporated sexithiophene films. *Adv. Mater.* **1993**, *5*, 461–464.
- (48) Servet, B.; Horowitz, G.; Ries, S.; Lagorsse, O.; Alnot, P.; Yassar, A.; Deloffre, F.; Srivastava, P.; Hajlaoui, R. Polymorphism and Charge Transport in Vacuum-Evaporated Sexithiophene Films. *Chem. Mater.* **1994**, *6*, 1809–1815.
- (49) de Boer, J. L.; van Smaalen, S.; Petricek, V.; Dusek, M.; Verheijen, M. A.; Meijer, G. Hexagonal close-packed C_{60} . *Chem. Phys. Lett.* **1994**, *219*, 469–472.

(50) Kowarik, S.; Gerlach, A.; Sellner, S.; Cavalcanti, L.; Konovalov, O.; Schreiber, F. Real-time X-ray diffraction measurements of structural dynamics and polymorphism in diindenoperylene growth. *Appl. Phys. A: Mater. Sci. Process.* **2009**, *95*, 233–239.

(51) Als-Nielsen, J.; McMorrow, D. *Elements of Modern X-ray Physics*, 2nd ed.; John Wiley & Sons: Chichester, U.K., 2011.

(52) Tolan, M. *X-ray Scattering from Soft-Matter Thin Films: Materials Science and Basic Research*; Springer Tracts in Modern Physics; Springer: Berlin, Germany, 1999.

(53) Birkholz, M. *Thin Film Analysis by X-Ray Scattering*; Wiley-VCH, Weinheim, Germany, 2006.

(54) Lorch, C.; Banerjee, R.; Frank, C.; Dieterle, J.; Hinderhofer, A.; Gerlach, A.; Schreiber, F. Growth of competing crystal phases of α -sexithiophene studied by real-time X-ray scattering. *J. Phys. Chem. C* **2015**, *119*, 819–825.

(55) Koini, M.; Haber, T.; Berkebile, S.; Koller, G.; Ramsey, M.; Resel, R.; Oehzelt, M. Growth of sexithiophene crystals on Cu(110) and Cu(110)-(2 × 1)O stripe phase - The influence of surface corrugation. *J. Cryst. Growth* **2009**, *311*, 1364–1369.

(56) Dürr, A. C.; Koch, N.; Kelsch, M.; Rühm, A.; Ghijsen, J.; Johnson, R. L.; Pireaux, J.-J.; Schwartz, J.; Schreiber, F.; Dosch, H.; Kahn, A.; et al. Interplay between morphology, structure, and electronic properties at diindenoperylene-gold interfaces. *Phys. Rev. B: Condens. Matter Mater. Phys.* **2003**, *68*, 115428(1–12).

(57) Salzmann, I.; Duhm, S.; Opitz, R.; Johnson, R. L.; Rabe, J. P.; Koch, N. Structural and electronic properties of pentacene-fullerene heterojunctions. *J. Appl. Phys.* **2008**, *104*, 114518 (1–11).